BIOMATERIALS

Dynamic DNA material with emergent locomotion behavior powered by artificial metabolism

Shogo Hamada[1]*, Kenneth Gene Yancey[1], Yehudah Pardo[2], Mingzhe Gan[3], Max Vanatta[4†], Duo An[1], Yue Hu[1], Thomas L. Derrien[1], Roanna Ruiz[1], Peifeng Liu[1,5,6], Jenny Sabin[4], Dan Luo[1,3,6,7]*

Copyright © 2019 The Authors, some rights reserved; exclusive licensee American Association for the Advancement of Science. No claim to original U.S. Government Works

Metabolism is a key process that makes life alive—the combination of anabolism and catabolism sustains life by a continuous flux of matter and energy. In other words, the materials comprising life are synthesized, assembled, dissipated, and decomposed autonomously in a controlled, hierarchical manner using biological processes. Although some biological approaches for creating dynamic materials have been reported, the construction of such materials by mimicking metabolism from scratch based on bioengineering has not yet been achieved. Various chemical approaches, especially dissipative assemblies, allow the construction of dynamic materials in a synthetic fashion, analogous to part of metabolism. Inspired by these approaches, here, we report a bottom-up construction of dynamic biomaterials powered by artificial metabolism, representing a combination of irreversible biosynthesis and dissipative assembly processes. An emergent locomotion behavior resembling a slime mold was programmed with this material by using an abstract design model similar to mechanical systems. Dynamic properties, such as autonomous pattern generation and continuous polarized regeneration, enabled locomotion along the designated tracks against a constant flow. Furthermore, an emergent racing behavior of two locomotive bodies was achieved by expanding the program. Other applications, including pathogen detection and hybrid nanomaterials, illustrated further potential use of this material. Dynamic biomaterials powered by artificial metabolism could provide a previously unexplored route to realize "artificial" biological systems with regenerating and self-sustaining characteristics.

INTRODUCTION

Characteristic properties of life, such as dynamic self-generation of organisms, are sustained by metabolism (*1*). Using a flux of matter and energy, molecules are irreversibly synthesized from ingredients and then further dynamically assembled into macromolecules and beyond by series of biological reactions, resulting in the structural hierarchy of life's materials (*2*–*4*). Mimicking metabolism as a material generation system may lead to the engineering of novel dynamic biomaterials with characteristic properties of life. Although various approaches have been reported to bioengineer such dynamic materials, mimicking metabolism from the ground up is still under development. For instance, engineered living materials allow material generation by life (*5*, *6*). However, this approach relies on external living systems, such as cells, to generate the material. Similarly, other dynamic biomaterials, such as active cytoskeletons, directly use already-existing metabolism designed by life (*7*–*10*). In general, although bioengineering approaches have the potential to create novel dynamic biomaterials with sophisticated active behaviors, the current approaches are built upon, and thus fundamentally limited by, life's existing metabolism. Chemical approaches have opened synthetic routes to build dynamic materials from scratch using chemical reactions, ultimately allowing flexibility in design (*11*–*14*). In particular, dissipative self-assembly (*15*–*19*) enabled out-of-equilibrium assembly of chemically synthesized components with a flux of energy, which can be regarded as an equivalent to the assembly process in metabolism. Inspired by this approach, we developed our concept of "artificial metabolism" to realize a new class of dynamic biomaterials with active behaviors. Analogous to the metabolism found in nature, our approach allows autonomous and dynamic generation of biomaterials with structural hierarchy by simultaneously coupling both irreversible synthesis/decomposition and dissipative assembly processes but in an artificial fashion. Our artificial metabolism was engineered upon a biological foundation using biomolecules and bioreactions but was not bound to the restrictions of life itself because of the bottom-up design of biochemical synthesis combined with assembly.

As a realization of this concept, we engineered a mechanism termed DASH—DNA-based Assembly and Synthesis of Hierarchical materials—providing a mesoscale approach to create dynamic materials from biomolecular building blocks using artificial metabolism (Fig. 1A). DASH was developed on the basis of nanotechnology that uses DNA as a generic material (*20*–*23*) ranging from nanostructures to hydrogels (*24*–*27*), for enzymatic substrates (*28*, *29*), and as linkers between nanoparticles (*30*–*32*). Analogous to the materials in living organisms, materials generated by DASH were synthesized and assembled into precoded patterns via anabolism. Furthermore, by integrating anabolism (generation) with catabolism (degeneration), the generated patterns were autonomously degenerated and also regenerated cyclically in situ by combining both generation and degeneration in an ordered fashion, responding to a built-in spatiotemporal feedback. Representing the behavior as a finite-state automaton (FSA; also known as a finite-state machine), an abstract model commonly used in robotics to describe states and state transitions of the machine

[1]Department of Biological and Environmental Engineering, Cornell University, Ithaca, NY 14853, USA. [2]Meinig School of Biomedical Engineering, Cornell University, Ithaca, NY 14853, USA. [3]CAS Key Laboratory of Nano-Bio Interface, Suzhou Institute of Nano-Tech and Nano-Bionics, Chinese Academy of Sciences, Suzhou 215123, China. [4]Department of Architecture, Cornell University, Ithaca, NY 14853, USA. [5]State Key Laboratory of Oncogenes and Related Genes, Shanghai Cancer Institute, Renji Hospital, School of Medicine, Shanghai Jiao Tong University, Shanghai 200032, China. [6]Micro-Nano Research and Diagnosis Center, Renji Hospital, School of Medicine, Shanghai Jiao Tong University, Shanghai 200127, China. [7]Kavli Institute at Cornell for Nanoscale Science, Cornell University, Ithaca, NY 14853, USA.
*Corresponding author. Email: hamada@cornell.edu (S.H.); dan.luo@cornell.edu (D.L.)
†Present address: Graduate School of Design, Harvard University, Cambridge, MA 02138, USA.

Downloaded from https://www.science.org at The Hong Kong University of Science and Technology (Guangzhou) on May 26, 2026

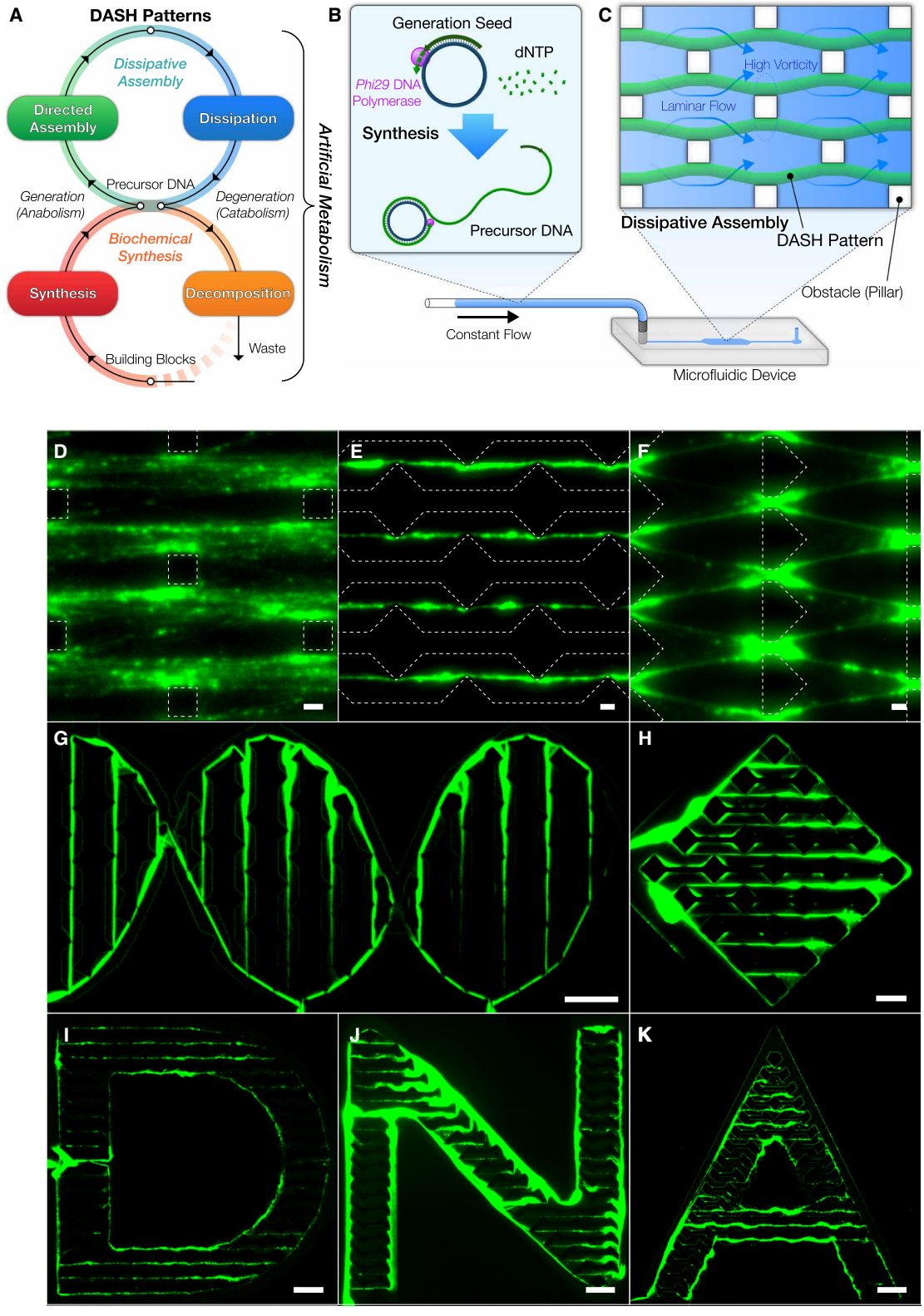

Fig. 1. DASH and the generated materials. (**A**) Schematics of DASH illustrates anabolic and catabolic pathways of artificial metabolism. (**B** and **C**) Implementation of DASH. (B) Synthesis of precursor DNA by RCA. (C) Formation of the DASH patterns by dissipative assembly using the flow with obstacles in microfluidic devices. (**D** to **K**) Generated DASH patterns. (D) 1D lines with a maximum width of 15 μm. (E) 1D lines with minimum width. (F) 2D cross-hatch patterns. (G) 2D drawings (double helix pattern). (H) 2D drawings (square). (I to K) 2D drawings (D, N, and A letter shapes). Dashed lines in (D) to (F) indicate the boundaries of obstacles. See fig. S42 for further details of the design. Scale bars, 10 μm (D to F), 100 μm (G), 50 μm (H), 100 μm (I to K). All flow rates, 0.1 μl/min.

Downloaded from https://www.science.org at The Hong Kong University of Science and Technology (Guangzhou) on May 26, 2026

(*33*), allowed further programming of the behavior as a machine. To further demonstrate the application of this material as a machine powered by artificial metabolism, we programmed an emergent "locomotion" behavior from a polarized regeneration process as a series of FSAs. The design was also expanded to realize an emergent "racing" behavior of two locomotive bodies by programming a simple interference between series of FSAs.

RESULTS

The anabolic pathway of DASH consists of two key simultaneous and autonomous processes to represent the concept of artificial metabolism: (i) biochemical synthesis of DNA molecules as a precursor of the material accomplished by an in situ enzymatic reaction and (ii) dissipative assembly of precursors to form the material with precoded patterns and shapes by flow. Specifically, in the process of precursor synthesis, in situ DNA synthesis was accomplished by rolling circle amplification (RCA) using Phi29 DNA polymerase, in a generation mix that also contained seeds (DNA templates with primers) and building blocks (Fig. 1B and figs. S1 and S2) (*27*, *34*). During the process of dissipative assembly, specific patterns were directly assembled (*35*) from precursor DNA using flow in microfluidic devices. Specifically, the generation mix was continuously infused into a microfluidic device with precisely spaced obstacles to assemble precursor DNA into precoded, specific patterns (Fig. 1C and figs. S3, S4, and S7). DASH thus achieved the aforementioned anabolic pathway by autonomously generating the material with structural hierarchy across scales (*3*, *4*): starting from nanoscale building blocks to polymer precursors, micrometer-scaled networks (hydrogels), and last, mesoscale patterns and shapes, all via simultaneous processes (figs. S10 and S11 and Supplementary Text).

Experimentally, a wide variety of mesoscale patterns and shapes, from periodically patterned one-dimensional (1D) lines to 2D arbitrary shapes, were generated to demonstrate the anabolic pathway of the material (Fig. 1, D to K, and figs. S5 and S42). The pathway enabled autonomous generation of patterned materials by organizing 1D, micrometer-thick fibrous DNA networks. Aided by computational fluid dynamics (CFD) simulations, we found that these DASH patterns could be deterministically designed on the basis of two simple guidelines: The patterns were predicted by taking the shortest route within the channel and by connecting adjacent pillars (obstacles), both in accordance to the direction of flow. To simplify the process, we designed microfluidic devices by a simple combinatory rule using seven types of structural units (fig. S6). The combination of units codes the location of pillars along with the routes of flow in the device to satisfy both guidelines, enabling a general design strategy for the DASH patterns.

Confocal fluorescence microscopy and scanning electron microscopy (SEM) revealed detailed morphologies of the generated material. Confocal microscopy of 2D cross-hatch patterns showed that the materials were formed in the middle of the microfluidic chamber (away from top and bottom of the chamber) with a fibrous morphology (Fig. 2, A and B). SEM observations revealed more detailed morphologies (Fig. 2, C and D): The fibrous structures were made of anisotropic bundles of DNA networks in which the orientation coincided with the direction of flow. Here, a device with 1D line patterns was chosen because of its easier transfer for the observation. Most of the materials were localized at the side edge of the pillars parallel to the flow direction and in the space between them, with little discernible DNA wrapped around the pillars. In addition, SEM observations revealed spherical structures with an average diameter of ~0.3 μm embedded inside the networks (fig. S12), similar to our earlier reports on physically entangled DNA hydrogels (*27*). However, here, anisotropic networks were evident between the spherical structures but not in the DNA hydrogel, presumably because of the directional flows.

To better understand the mechanism behind the pattern generation by DASH, we recorded and quantified time-lapse videos (Fig. 2E and movies S1 and S2). The existence of elapsed time between flow initiation and the onset of the pattern generation suggested that the network formation depended on a minimum molecular weight of synthesized precursor DNA (e.g., an estimated molecular weight of 3.3×10^7 in the case of 2D cross-hatch patterns with 5 nM of generation mix; Supplementary Text). We observed that network formation was initiated from the side edges of the pillars in the middle (i.e., center of the *z* axis) of the chamber, and then, with additional generations, these DNA networks started to be connected into one continuous fibrous structure between pillars. If the dominant mechanism was wrapping DNA networks around the pillars, then the fibrous morphology should have started from the upstream edge instead of the side edges of the pillars, and the overall pattern generation should have started from the upstream region of the device (*36*). Our observation indicated otherwise; the side edges of the pillars were the main places where the assembly was initiated. Thus, we hypothesized that the assembly mechanism of the DASH patterns was a combination of two processes: the formation of the DNA network triggered at the side edges of the pillars and the redistribution of preformed networks (both in situ and in flowing solution) into continuous, fibrous anisotropic structures along the direction of flow. The time-lapse images illustrate that the thickness of the structures increased in the later stages with the gaps between pillars eventually filled with the DNA networks. This additional thickening strongly suggested that the redistribution of excess DNA networks formed in solution happened later in the process of the pattern formation rather than earlier.

To investigate the underlying mechanisms of the assembly process, we first performed CFD simulations and then experimentally verified them from two aspects: the formation of new networks and the redistribution of preformed networks into a fibrous morphology (Fig. 2, F to H, and movie S3). We chose the DASH patterns with 1D lines for the comparison because of its geometric simplicity. For the formation, we found that the sides of the pillars corresponded to areas of high vorticity (Fig. 2H). These results along with the sensitivity measurements (figs. S13 to S17 and Supplementary Text) and a pillar shape comparison experiment (figs. S18 to S20 and Supplementary Text) suggested that the flow, particularly the vorticity, was critical in the formation process by locally and dynamically triggering a physical entanglement of DNA into networks at the side of pillars. In short, a higher magnitude of vorticity at the side of pillars led to an earlier generation starting time. Similar vorticity-triggered structure formation observed in biofilms and proteins also supported our hypothesis (*37*, *38*). For the redistribution, an overlay of time-lapse videos with simulations of flow velocity showed that the fibrous structure was formed along the direction of flows in the region of highest velocity, consistent with the redistribution mechanism (Fig. 2, F and G, and movie S3). Therefore, the mechanism behind the assembly was most likely a combination of the vortex-induced dynamic formation of new networks and the flow-directed redistribution of preformed networks.

Downloaded from https://www.science.org at The Hong Kong University of Science and Technology (Guangzhou) on May 26, 2026

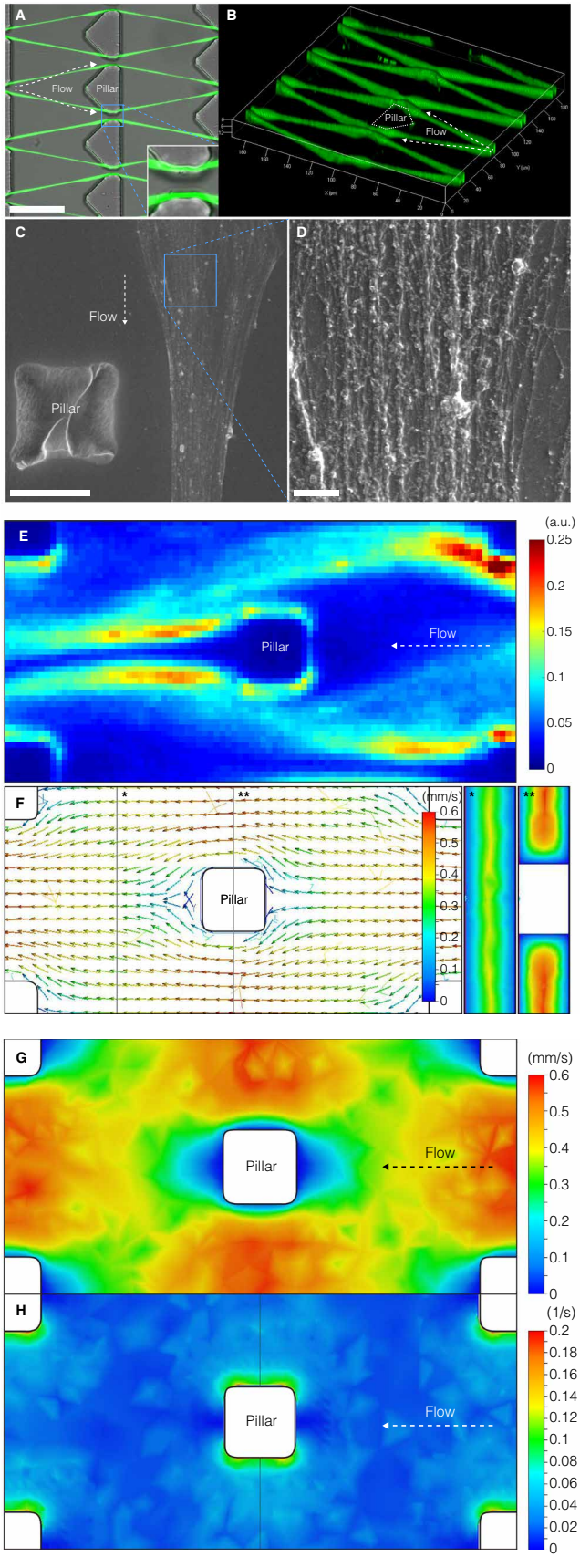

Fig. 2. Detailed morphology and hydrodynamics studies of the DASH patterns. (**A** to **D**) Detailed images of the DASH pattern. (A) An overlay of bright-field and green fluorescence channel by confocal fluorescence microscopy, showing both pillars and the DASH patterns. Scale bar, 50 μm. (B) Reconstructed 3D image of (A). Dashed line indicates the boundary of the pillar. (C) SEM observation of the DASH pattern. Scale bar, 10 μm. (D) Close-up image of (C). Anisotropic networks with embedded spherical structures were observed. Scale bar, 1 μm. (**E** to **H**) Hydrodynamics studies of the DASH pattern generation. (E) A snapshot from the time-lapse video recording of the generation process (experimental result). a.u., arbitrary units. (F to H) CFD simulation results. (F) Flow velocity vector map. Side subfigures represent sections at corresponding locations indicated by asterisks. (G) Flow velocity heat map. (H) Flow vorticity heat map. Dashed arrows indicate the flow direction. All flow rates, 0.1 μl/min.

Integrating the above anabolic generation process with a catabolic degeneration process via DNA-hydrolyzing enzymes further expanded the metabolic pathways of the artificial metabolism. We used both anabolic and catabolic pathways to induce sequential generation and degeneration of the pattern at a static location. Here, the DASH patterns were autonomously generated and then synchronously and autonomously degenerated by a combination of enzymatic reactions and flows (Fig. 3, A to C, figs. S21 to S23, and movie S4). The reagents required for both generation and degeneration were simultaneously flowed into the microfluidic device. Crucially, once the flow started, both processes of generation and degeneration were executed without any external manipulation. A three-inlet microfluidic device was used with the center inlet containing the generation mix with DNA polymerase, whereas the inlets at either side contained the degeneration mix with the DNA-hydrolyzing enzyme, deoxyribonuclease (DNase) I. We described the overall behavior of the material by using an FSA with three states, Init, Growth, and Decay, with autonomous and sequential state transitions (Fig. 3B). This abstraction with discrete states and state transitions, similar to the methods used in mechanical robots, allowed interpretation of the overall behavior of the material as a machine and thus enabled further programming of the behavior mentioned below. The state transition between Growth and Decay was switched by a spatiotemporal feedback. CFD simulation illustrated the hydrodynamics during the process (fig. S24 and Supplementary Text). Initially, all three solutions flowing into the device remained laminar (Init). Thus, the degeneration mix was kept separated from the generation mix, and the anabolic process started at the center of the device (Growth). Gradually, accumulation by redistributed DNA networks started to fill the gap between the pillars, substantially altering the flow dynamics. This spatiotemporal feedback allowed both the generation and the degeneration solutions to be mixed, thus triggering the state transition. The catabolic process then started to dominate, and last, the materials were degenerated (Decay). Additional experimental tests showed that the sequential occurrence of generation and degeneration (cyclical regeneration) could be autonomously repeated at least two times when the DNA synthesis time was kept constant (figs. S25 to S28, movie S5, and Supplementary Text), demonstrating that both anabolic and catabolic pathways could be seamlessly integrated and regulated in a regenerative fashion without any interference from outside.

On the basis of the dynamic generation and degeneration behaviors of the material at the static location, we then programmed a locomotive behavior powered by artificial metabolism using DASH (Fig. 3, D to F, and movie S6). Inspired by the shapes and migrating behaviors of pseudoplasmodia (slug) of the cellular slime mold

Downloaded from https://www.science.org at The Hong Kong University of Science and Technology (Guangzhou) on May 26, 2026

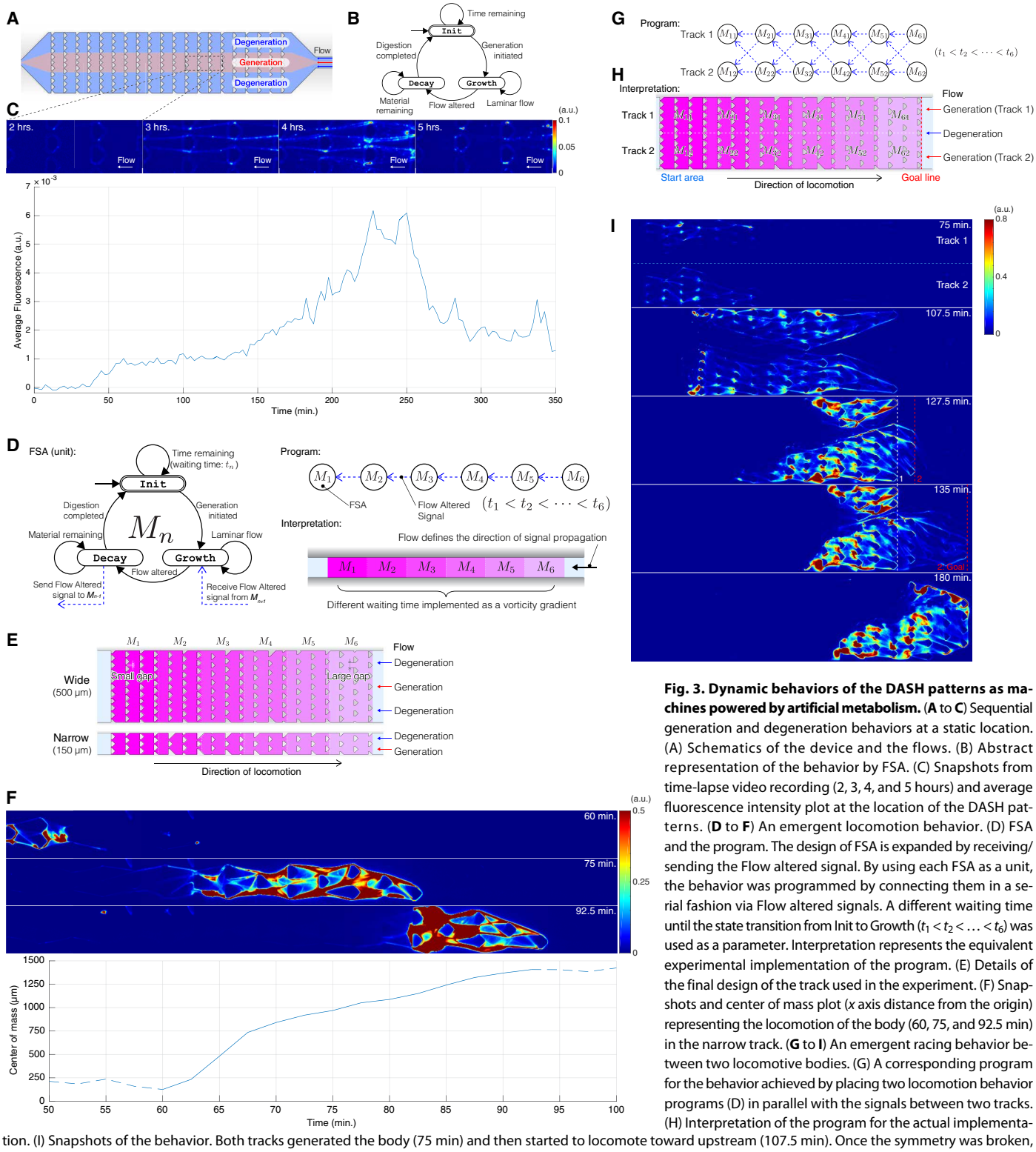

Fig. 3. Dynamic behaviors of the DASH patterns as machines powered by artificial metabolism. (**A** to **C**) Sequential generation and degeneration behaviors at a static location. (A) Schematics of the device and the flows. (B) Abstract representation of the behavior by FSA. (C) Snapshots from time-lapse video recording (2, 3, 4, and 5 hours) and average fluorescence intensity plot at the location of the DASH patterns. (**D** to **F**) An emergent locomotion behavior. (D) FSA and the program. The design of FSA is expanded by receiving/sending the Flow altered signal. By using each FSA as a unit, the behavior was programmed by connecting them in a serial fashion via Flow altered signals. A different waiting time until the state transition from Init to Growth ($t_1 < t_2 < \ldots < t_6$) was used as a parameter. Interpretation represents the equivalent experimental implementation of the program. (E) Details of the final design of the track used in the experiment. (F) Snapshots and center of mass plot (*x* axis distance from the origin) representing the locomotion of the body (60, 75, and 92.5 min) in the narrow track. (**G** to **I**) An emergent racing behavior between two locomotive bodies. (G) A corresponding program for the behavior achieved by placing two locomotion behavior programs (D) in parallel with the signals between two tracks. (H) Interpretation of the program for the actual implementation. (I) Snapshots of the behavior. Both tracks generated the body (75 min) and then started to locomote toward upstream (107.5 min). Once the symmetry was broken, the body at track 2 led the race (dashed line) and started to slow down the body at track 1 by degenerating the body (127.5 min). After the body at track 2 won the race by reaching the goal (135 min), the body at track 1 was completely degenerated (~180 min). Flow rates applied, 0.1 μl/min (C) and 0.15 μl/min (F and I) for both generation and degeneration mixes.

Downloaded from https://www.science.org at The Hong Kong University of Science and Technology (Guangzhou) on May 26, 2026

Dictyostelium discoideum (*39*), we programmed a behavior in which a slug-like body was generated by autonomous growth of the DASH patterns, followed by autonomous locomotion of the body along a track against a constant flow. The locomotion was realized as an emergent behavior based on continuous polarized regeneration: The front end generated its body, and the back end degenerated itself. At the abstract design level, the behavior was programmed by expanding the FSA introduced above in a serially connected manner (M_1 to M_6), regarding each FSA as an autonomous and modular unit (Fig. 3D). Each unit (M_n) could accept a "Flow altered" signal from an adjacent unit (M_{n+1}) that triggers the state transition from Growth to Decay and could also propagate the signal to the next (M_{n-1}). The locomotion behavior was programmed by setting different waiting times ($t_1 < t_2 < \ldots < t_6$) until the state transition between Init and Growth was triggered. Growth of each FSA started from M_1 according to the waiting time. Once the unit M_n changed its state to Decay because of its internal feedback, the Flow altered signal was propagated to the adjacent unit M_{n-1} and beyond, ensuring the state transition at the back end of the body. As a result, the direction of locomotion was represented as spatiotemporal delay of Growth and sequential state transition to Decay. Experimentally, similar multi-inlet channels containing generation and degeneration mixes were prepared as predefined tracks for the behavior (Fig. 3E). Here, the gap between adjacent pillars was tuned from small (downstream) to large (upstream) in a region-by-region fashion along the track. Each region corresponds to each FSA. The size of the gap that defines the magnitude of vorticity represents a parameter (waiting time) in each unit to trigger the state transition from Init to Growth. As programmed, this vorticity gradient elicited a spatiotemporal delay of the transition from Init to Growth state, starting from the downstream region of the track. In short, the direction of the locomotion is experimentally interpreted as a gradient in the magnitude of vorticity under the constant flow rate. We also emphasize here that the direction of locomotion was deliberately programmed to be against the flow direction in all examples. After the autonomous generation started at the downstream region and the body constituted by the DASH patterns started to grow, a spatial feedback due to the generated patterns triggered the transition to Decay state, also starting from downstream. The transition to the Decay state is also propagated to the downstream regions because of the flow (represented as a "Flow altered" signal sent to M_{n-1}), ensuring that catabolism would dominate in these regions. At the same time, the transition from Init to Growth state continued toward the upstream region (i.e., down the vorticity gradient). As a result, an overall locomotion behavior of the body along the track against the direction of flow emerged as programmed by a series of FSAs. The behavior was experimentally observed in straight (wide and narrow widths) and curved tracks (see movie S6), illustrating the design flexibility of the trajectory. The locomotion velocity was measured as 2.3 mm/hour with narrow tracks (Fig. 3F, fig. S29, and Supplementary Text).

To further demonstrate the application of the material as a machine, we expanded the design by using an abstracted programming method to achieve an emergent racing behavior of two competing bodies by two series of FSAs (Fig. 3G). Each series (M_{11} to M_{61} and M_{12} to M_{62}) was designed in the same manner as the previous emergent locomotion behavior; we further added a simple interference between two locomotive bodies. Specifically, we designed the state transition signal from Growth to Decay to also interfere between tracks (denoted by the arrows between two series of FSA); the faster moving body could affect and alter the state of another track to Decay, thus slowing down the locomotion of the body at the other track by triggering the degeneration. We interpreted this program as two tracks representing two series of FSA located side by side without any physical boundaries between each other (Fig. 3H). Experimentally, the design was implemented by simply inverting the types of flow (the generation mix on the outside and the degeneration mix on the inside) in a wide-width track introduced in the previous section. Because there was no boundary between the two tracks, the altered flow at one track could affect the state of the other track. The result successfully showed a competing race between two bodies with the winner at track number 2 (Fig. 3I and movie S7). As programmed, once the symmetry between two bodies was broken, presumably because of the randomness in flow and the body, Decay state caused by the leading body at track 2 affected the body at track 1, resulting in the degeneration of the body (see the snapshot at 127.5 min). After the body at track 2 reached the goal (135 min), the behavior ended with a complete degeneration of the body at track 1 (180 min).

Last, in addition to using the DASH material in machine applications, several other applications were developed. One of the applications was nucleic acid detection (fig. S30 and Supplementary Text). The goal of this application was to demonstrate the advantages of the material's self-generating characteristics. We prepared a generation seed that was amplifiable when and only when a target DNA/RNA was present in the sample. The anabolic characteristic of the material was thus converted to act as a selective amplification process only for targeted DNA/RNA. The generated DASH patterns were then read either by naked-eye observation or by a pattern recognition algorithm based on Fourier transform, using the mechanism as a binary readout method (fig. S8). Experimentally, we chose a target sequence taken from cucumber mosaic virus (CMV) as a model pathogen. The target was successfully detected at concentrations of 500 and 50 pM by recognizing the self-generated DASH patterns (Fig. 4A, figs. S31 to S33, and Supplementary Text). Non-targets with a mismatch of only 2 bp (base pair) did not generate the patterns, demonstrating the specificity of the detection method. Next, to illustrate the potential uses of self-generated materials, we created various hybrid functional materials from the DASH patterns. The DASH patterns served as a versatile mesoscale scaffold for a diverse range of functional nanomaterials beyond DNA, ranging from proteins to inorganic nanoparticles, such as avidin (Fig. 4B, figs. S34 and S35, and Supplementary Text), quantum dots (Fig. 4C, fig. S36, and Supplementary Text), and DNA-conjugated gold nanoparticles (AuNPs) (Fig. 4D, figs. S37 and S38, and Supplementary Text). The generated patterns were also rendered functional with catalytic activity when conjugated with enzymes (figs. S39 and S40 and Supplementary Text). We also showed that the DNA molecules within the DASH patterns retained the DNA's genetic properties and that, in a cell-free fashion, the materials themselves successfully produced green fluorescent proteins (GFPs) by incorporating a reporter gene for *sfGFP* (Fig. 4E and figs. S9 and S41) (*40*). The protein production capability of the materials established the foundation for future cell-free production of proteins, including enzymes, in a spatiotemporally controlled manner.

CONCLUSION

We have created a dynamic material powered by artificial metabolism using simultaneous processes of biochemical synthesis and dissipative

Downloaded from https://www.science.org at The Hong Kong University of Science and Technology (Guangzhou) on May 26, 2026

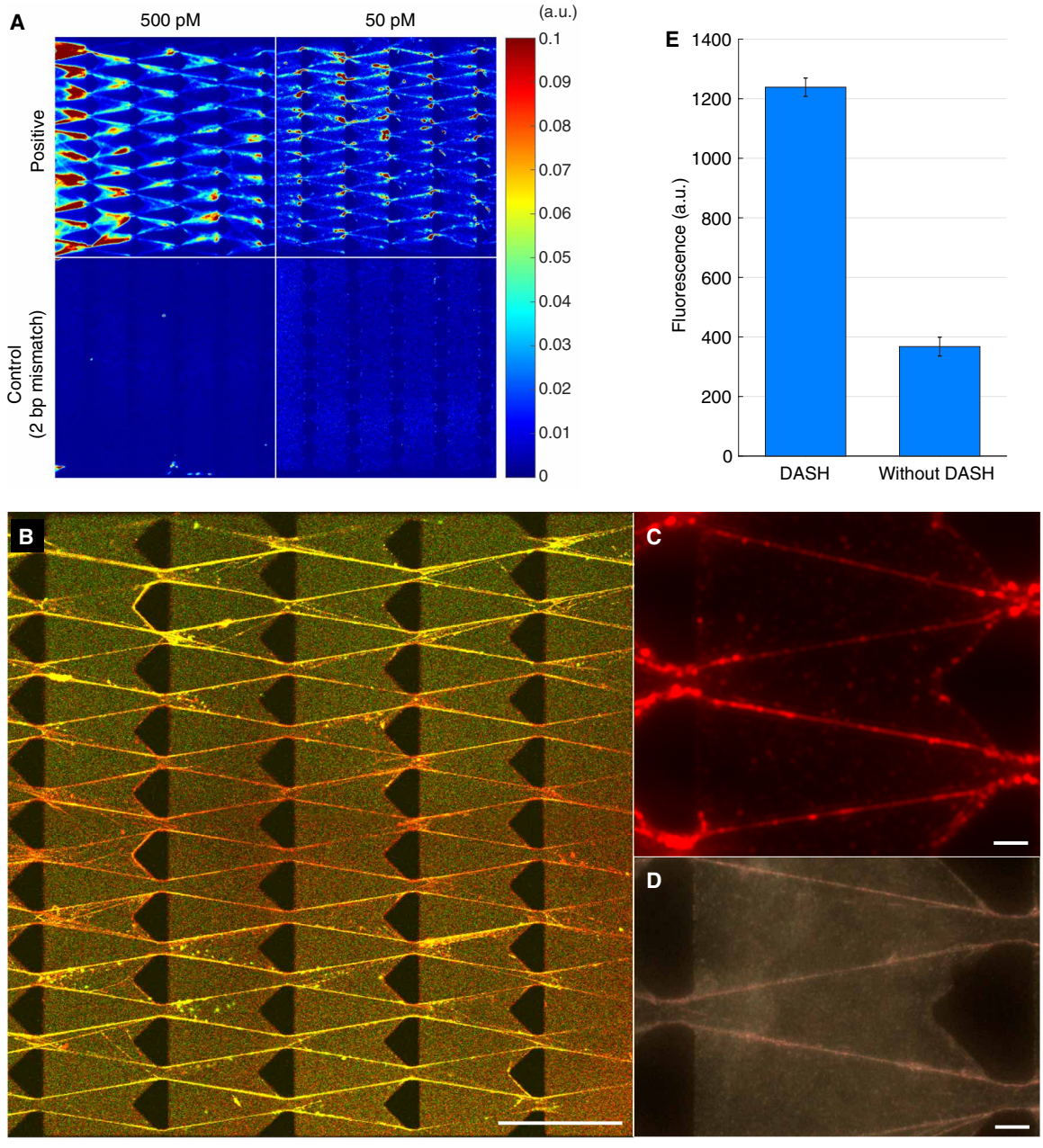

Fig. 4. Other applications of the DASH material. (**A**) Pathogen DNA/RNA detection by the generated DASH patterns. Positive samples at 500 and 50 pM were successfully detected by the generated patterns. Control samples using nontarget sequences with 2-bp mismatch resulted in no pattern generation. (**B** to **D**) Hybrid materials. (B) Fluorescent molecule–conjugated avidin binding. A gradient of two colors was achieved by using three-inlet device [center flow, Texas Red (red); side flow, FITC (green)]. Scale bar, 100 μm. (C) Quantum dot attachments mediated by avidin binding. Scale bar, 10 μm. (D) DNA-conjugated AuNP attachments on the DASH patterns, observed by dark-field microscopy. Scale bar, 10 μm. (**E**) CFPE from the DASH patterns incorporating a reporter gene for *sfGFP*. Error bars represent SD. All flow rates applied during the DASH pattern generation, 0.1 μl/min.

assembly. Our implementation of the concept, DASH, successfully demonstrated various applications of the material. We succeeded in constructing machines from this novel dynamic biomaterial with emergent regeneration, locomotion, and racing behaviors by programming them as a series of FSAs. Bottom-up design based on bioengineering foundations without restrictions of life fundamentally allowed these active and programmable behaviors. It is not difficult to envision that the material could be integrated as a locomotive element in biomolecular machines and robots (*29*, *41*–*50*). The DASH patterns could be easily recognized by naked eyes or smartphones, which may lead to better detection technologies that are more feasible in point-of-care settings. DASH may also be used as a template for other materials, for example, to create dynamic waves of protein expression or nanoparticle assemblies. In addition, we envision that further expansion of artificial metabolism may be used for self-sustaining structural components (*51*) and self-adapting substrates for chemical

Downloaded from https://www.science.org at The Hong Kong University of Science and Technology (Guangzhou) on May 26, 2026

production pathways (*52*). Ultimately, our material may allow the construction of self-reproducing machines (*53*) through the production of enzymes from generated materials that, in turn, reproduce the material (*54*). Our biomaterial powered by artificial metabolism is an important step toward the creation of "artificial" biological systems with dynamic, life-like capabilities.

MATERIALS AND METHODS

Materials

RepliPHI Phi29 DNA polymerase, 10× RepliPHI buffer [400 mM tris-HCl (pH 7.5), 500 mM KCl, 100 mM $MgCl_2$, 50 mM $(NH_4)_2SO_4$, and 40 mM dithiothreitol], and deoxynucleotides (dNTPs) were obtained from Epicentre (Madison, WI). T4 DNA ligase, exonuclease I, and exonuclease III were obtained from New England BioLabs (Ipswich, MA). Adenosine triphosphate (ATP) was obtained from Teknova (Hollister, CA). Oligonucleotides were chemically synthesized and purified using standard desalting method by Integrated DNA Technologies (Coralville, IA). GelRed Nucleic Acid Gel Stain and nuclease-free water were obtained from VWR International (Radnor, PA). SYBR Green I, 40% acrylamide/Bis (19:1), ammonium persulfate, and a polydimethylsiloxane (PDMS) silicone elastomer kit (Sylgard 184, Dow Corning) were obtained from Thermo Fisher Scientific (Waltham, MA). Tetramethylethylene diamine was obtained from Sigma-Aldrich (St. Louis, MO). Other additional materials used in specific experiments were described in other sections and in the Supplementary Materials accordingly.

Generation mix preparation

Generation seeds were prepared by circularizing template DNA with primer DNA (fig. S1). First, chemically synthesized template and primer DNAs were mixed in 1× RepliPHI reaction buffer at final equimolar concentration of 1 μM and then annealed from 95° to 4°C (−1°C/min) by thermal cycler. T4 DNA ligase (200 U) and ATP (final concentration, 1.25 mM) were added and then incubated overnight at 4°C (total volume, 20 μl; final seed concentration, 0.5 μM) for the reaction. Ligated generation seed solution with a final concentration of 5 nM (or otherwise mentioned) was then mixed on ice with 1 mM each of dNTP, 1× SYBR Green I, and Phi29 (5.7 U/μl) in 1× RepliPHI reaction buffer for the generation mix.

Microfluidic device design

The devices were designed by following three steps. First, a layout of the final DASH patterns was roughly determined. Next, obstacles were assigned by following the patterns using an abstracted method based on node-link diagrams. A total of seven types of standard structural units were used for the design. Last, the main chamber design was connected to inlet/outlet channels. See Additional Materials and Methods in the Supplementary Materials for a detailed design process.

Experimental setup of the devices

Simultaneous synthesis and assembly using microflow were embodied by a combination of microfluidic device connected to tubing and syringe (fig. S7). Prepared generation mix solution was drawn into Cole-Parmer Microbore Puri-Flex Autoanalysis Tubing (Vernon Hills, IL) connected to 1-ml BD Medical tuberculin syringe (Franklin Lakes, NJ) and short Microgroup hypodermic tubing (Medway, MA) as an insertion tip. Immediately after preparing the solution, the syringe was then set to a Harvard Apparatus PHD-2000 syringe pump (Holliston, MA) and infused. Before the experiment, DASH devices were prefilled by nuclease-free water; both inlets and outlets were also covered by water. Once the generation mix emerged at the tip, the tip was immediately inserted to the DASH device. The device and the tip were both covered by solution to ensure that no air bubbles entered the device during the process. Typically, generation mix was infused to the DASH device at 0.1 μl/min.

A three-inlet design (fig. S42, no. 14-2) was designed for generation and degeneration experiments. The center inlet was connected to the generation solution (final seed concentration, 0.1 nM). Side inlets were connected to degeneration solution [DNase I (1 U/μl) in 1× Phi29 reaction buffer]. Both generation and degeneration solutions were infused at 0.1 μl/min. For the emergent locomotion experiments, two- and three-inlet tracks with gradient vorticity regions (fig. S42, nos. 22-3, 23-3, and 23-4) were used. Both solutions were infused at 0.15 μl/min. For the emergent racing experiments, three-inlet tracks with gradient vorticity regions (fig. S42, no. 23-3) were used. Both solutions were infused at 0.15 μl/min.

Fluorescence microscopy

Fluorescence microscopy images used for morphological studies and quantitative analyses were taken by Olympus BX-61 microscope (Japan) with Sutter Instrument Lambda LS Xenon light source (Novato, CA). Green fluorescence [excitation (Ex.), 484 nm; emission (Em.), 520 nm], red fluorescence (Ex., 555 nm; Em., 605 nm), and red quantum dot (Ex., 420 nm; Em. 605 nm) filters were purchased from Chroma Technology Corporation (Bellows Falls, VT). Objective lenses (4× and 10×) by Olympus (Tokyo, Japan) were used. Exposure time of the bright-field channel was set to 100 ms; fluorescence channels were set to 2000 ms throughout all experiments. Time-lapse videos were taken using 150 s per frame [except the short observation interval video (15 s per frame) in movie S6] with 4× objective lens. Images including raw data were captured by Intelligent Imaging Innovations SlideBook (Denver, CO). Raw data (16-bit tiff files) were imported and processed by in-house software for detailed observation.

Confocal laser scanning microscopy images and the *z*-stacked videos were taken by two confocal laser scanning microscopes [Zeiss LSM710 (Germany) and Olympus IX-81 (Japan)]. For the time-lapse video recording (movie S2), device no. 9-1 (fig. S42) was chosen with a final concentration of 5 nM of generation mix. A 10× objective lens was chosen for the observation because of focal length. A filter (Ex., 488 nm; Em., 520 nm) was used for the green fluorescence channel. The capture interval was set to 110 s; a total of 30 frames were recorded. Thirty layers (*z* axis) were taken for each stack.

Scanning electron microscopy

After the generation of the DASH patterns, 4% paraformaldehyde fixative (Electron Microscopy Sciences, Hatfield, PA) was flowed into the device (0.1 μl/min) for 10 min. After fixation for 24 hours at 4°C, the device was opened, and the pattern was fixed on the PDMS substrate. Upon rinsing with nuclear-free water, the pattern was dehydrated in a series of graded ethanol (10, 25, 50, 75, 90, and 100%) and immersed in 100% ethanol. Subsequently, the pattern was dried with critical point drying process using Bal-Tec (Leica) CPD 408 (Germany) and then examined with LEO (Zeiss) 1550 FESEM (Germany).

Downloaded from https://www.science.org at The Hong Kong University of Science and Technology (Guangzhou) on May 26, 2026

CFD simulation

2D CAD files were exported to DXF format from the original CAD design (GDSII) and then imported to Rhinoceros 3D (Robert McNeel & Associates, Seattle, WA) and simulated using Autodesk Simulation CFD (San Rafael, CA). Within Rhinoceros 3D, the original 2D CAD file was extruded into a 3D volume with the height that corresponds to the actual DASH devices. The model was then exported as a STEP file to be imported in the preparation software within the CFD software. For the fluid flowing through the geometry, the default water profile was used for simplification (table S2A). For the solid structures, properties similar to the existing default material of silicone rubber were applied (table S2B). The simulations were run for a maximum of 500 iterations or until the result reached convergence (automatically detected and halted by Autodesk CFD software). Three methods were used for the result visualization of the simulations: heat maps, vector fields, and particle traces. Heat maps and vector fields were normalized between all results to maintain uniformity and were located at 8 μm from the bottom of the volume (midpoint).

DASH-based pathogen detection

A sequence taken from CMV was used for the target. A total mismatch of 2 bp (1 bp at each side of the ligation site) of sequence alternation were made for the nontarget. For simplification of the experiment, the total target sequence length was shortened to 33 nucleotide oligomers; chemically synthesized single-strand DNA was used instead of RNA. Recognition was performed by adding target DNA to a solution containing template and primer DNA in 1× RepliPHI Phi29 buffer. After the annealing process (from 95°C to room temperature at −1°C/min), T4 DNA ligase (final concentration, 10 U/μl) was added along with 1.19 mM ATP, and the reaction was left overnight at 4°C. Generation mix for the amplification (DASH pattern generation) was then prepared by following the standard method with corresponding concentration of ligated template-primer mix; the solution was then infused to the device (fig. S42, no. 9-1) at 0.1 μl/min. For a maximum of 4 hours, time-lapse video was recorded during the process; the results were then imported using an in-house software.

DASH-avidin/streptavidin hybrid materials

The DASH pattern was generated using the standard protocol with a zigzag pattern device (fig. S42, no. 9-1) over periods of 1 hour to 1 hour and 20 min. Immediately after DASH generation, a solution (50 μg/ml) of either Texas Red–conjugated avidin or Texas Red–conjugated streptavidin in 1× RepliPHI reaction buffer was flowed through the device at 0.1 μl/min for 1 hour. Fresh 1× RepliPHI reaction buffer was then flowed through the device for 30 min to remove any unbound protein before imaging.

For two-colored avidin binding, to ensure that the DASH patterns formed evenly throughout the entire device, DASH generation solution was pumped through all inlets simultaneously (each at 0.1 μl/min). To avoid spectral overlap with fluorescein isothiocyanate (FITC)–conjugated avidin, SYBR Green I was not included in the generation mix. After DASH formation, Texas Red–conjugated avidin (50 μg/ml) and FITC-conjugated avidin (50 μg/ml) were pumped simultaneously into the device (one avidin conjugate per inlet) at 0.1 μl/min each for 1 hour. Before imaging, the device was flushed with 1× Phi29 reaction buffer for 15 to 30 min to reduce background.

DASH-quantum dots hybrid materials

The DASH pattern was generated using the standard protocol over a period of 1 hour and 30 min without SYBR Green I. Immediately after DASH generation, a solution (250 μg/ml) of FITC-conjugated avidin (Thermo Fisher Scientific, Waltham, MA) in 1× RepliPHI reaction buffer was flowed through the device at 0.1 μl/min for 1 hour and then followed by final 0.2 μM biotin-labeled Qdot 605 nanocrystals (Thermo Fisher Scientific, Waltham, MA) in 1× RepliPHI reaction buffer for 10 to 30 min. Control samples were tested without FITC-conjugated avidin.

DASH-AuNP hybrid materials

Citrate-coated 40- and 5-nm AuNPs were purchased from Ted Pella (Redding, CA). The oligonucleotides used were ordered conjugated with a 5′ thiol group from Integrated DNA Technologies, which was activated before attachment by deprotection using tris(2-carboxyethyl)phosphine hydrochloride (TCEP). The oligonucleotides were incubated at a ratio of 1:5 (DNA/TCEP). The deprotected DNA was then added to the AuNPs at DNA/AuNP ratios of 80:1 for the 5-nm AuNPs and 4200:1 for the 40-nm AuNPs to ensure maximum surface coverage, followed by overnight shaking at 500 rpm at room temperature. NaCl was then slowly added over a period of 8 hours to a final concentration of 500 mM, reducing DNA-DNA repulsion and further increasing the DNA coverage. The nanoparticles were then purified of salt and excess DNA by five rounds of centrifugation in nuclease-free water.

The DASH pattern was generated using the standard protocol using device no. 9-1 (fig. S42). After 70 min of generation, DNA-conjugated 5- or 40-nm AuNP solution with final 1× RepliPHI buffer was flowed inside the device (0.1 μl/min) for 45 min. The process was constantly monitored with a microscope to ensure sufficient attachment of nanoparticles.

Cell-free protein expression

The DASH pattern generation was performed by following a protocol similar to the standard protocol, with a final seed concentration of 15 nM with 8 mM mix of dNTP, RepliPHI Phi29 DNA polymerase (4 U/μl), and Hoechst 33342 (0.5 μg/ml) in 1× RepliPHI buffer (see the Supplementary Materials for the generation seed preparation). Blue Hoechst dye was used to stain DNA for the confirmation of DASH pattern generation instead of SYBR Green I to not overlap with the green emission wavelength of *sfGFP* for the subsequent protein expression steps. The generation process was monitored by time-lapse observation until the pattern generation was complete.

After the DASH pattern generation process, a protein expression primer was infused at 0.1 μl/min for 60 min. The primer sequence was designed to bind T7 promoter regions present on the DASH patterns to activate protein expression. The S30 T7 High-Yield Protein Expression System from Promega (Madison, WI) was then used for the protein expression. Nuclease-free water, S30 Premix Plus, and S30 T7 Extract (both supplied with kit) were mixed in a ratio of 2.4:4:3.6 and infused at 0.1 μl/min. For the direct observation of cell-free protein expression (CFPE) in the DASH device, the pump was programmed to pause every 20 min to increase the residence time. For a quantitative measurement (Fig. 4E), a solution from a total of 2 hours of CFPE in the device was collected, and fluorescence was measured using the Synergy 4 Microplate Reader [with filters (Ex., 475 nm; Em., 508 nm)] from BioTek (Winooski, VT).

Downloaded from https://www.science.org at The Hong Kong University of Science and Technology (Guangzhou) on May 26, 2026

SUPPLEMENTARY MATERIALS

robotics.sciencemag.org/cgi/content/full/4/29/eaaw3512/DC1
Additional Materials and Methods
Supplementary Text
Fig. S1. Schematics of the generation seed preparation.
Fig. S2. Polyacrylamide gel electrophoresis of ligated templates with primers.
Fig. S3. Cross-sections of the DASH device.
Fig. S4. Overall device layout of the DASH device.
Fig. S5. Schemes for the "letter D" main chamber design.
Fig. S6. Standard structure elements of the DASH patterns.
Fig. S7. Experimental setup of the DASH generation.
Fig. S8. Overall process of DASH data analysis software.
Fig. S9. Polyacrylamide gel electrophoresis of original double-stranded plasmid and single-stranded template after nicking enzyme and exonuclease treatment.
Fig. S10. Redistribution of long DNA without simultaneous synthesis.
Fig. S11. Redistribution of generation mix after 2.5-hours synthesis reaction, stopped with Proteinase K.
Fig. S12. SEM image used for the spherical structure analysis.
Fig. S13. CFD simulation of velocity mapping inside a three-chamber device.
Fig. S14. CFD simulation of vorticity mapping inside a three-chamber device.
Fig. S15. Sample signal-to-noise ratio (SNR) data used for the generation starting time analysis.
Fig. S16. A relation between characteristic flow velocity and vorticity obtained by CFD simulation.
Fig. S17. A relation between vorticity and inverse of frame number of DASH generation starting time.
Fig. S18. Flow velocity heat map of two devices with different pillar shapes.
Fig. S19. Flow vorticity heat map of two devices with different pillar shapes.
Fig. S20. Pillar shape comparison of the DASH pattern generation.
Fig. S21. Intensity plot from three sample points during generation and degeneration of the DASH patterns.
Fig. S22. Location of three sample points used in fig. S21.
Fig. S23. Average intensity from the rectangle area (x = 700 to 740 px, y = 120 to 190 px) during generation and degeneration of the DASH patterns.
Fig. S24. CFD simulation (particle trace) during generation and degeneration processes.
Fig. S25. Repeated generation and degeneration of the DASH patterns at the static location.
Fig. S26. Intensity plot from three sample points during repeated generation and degeneration of the DASH patterns at the static location.
Fig. S27. Location of three sample points used in fig. S26.
Fig. S28. Average intensity plot from rectangular region (x = 820 to 851 px, y = 140 to 147 px) during repeated generation and degeneration of the DASH patterns at the static location.
Fig. S29. Emergent locomotion behavior (wide track width, device no. 22-3).
Fig. S30. Schematics of DNA/RNA detection.
Fig. S31. Signal-to-noise ratio (SNR) of the generated DASH patterns from target samples.
Fig. S32. Signal-to-noise ratio (SNR) of the generated DASH patterns from non-target samples.
Fig. S33. Average intensity versus SNR of the DASH patterns with positive and non-target samples.
Fig. S34. DASH-avidin binding results.
Fig. S35. DASH-streptavidin binding results.
Fig. S36. DASH-quantum dot (Qdots) attachment result.
Fig. S37. DASH-AuNP patterns.
Fig. S38. SEM observation of DASH-AuNP patterns.
Fig. S39. Avidin–horseradish peroxidase (HRP) activity verification using 3,3′,5,5′-tetramethylbenzidine (TMB) substrate.
Fig. S40. Observation of avidin-HRP activity in the DASH device.
Fig. S41. Direct observation of CFPE from the DASH patterns.
Fig. S42. DASH device and track design catalog.
Tables S1. Sectional height measurement data of DASH devices.
Tables S2. Material settings used for CFD simulation.
Tables S3. Vorticity at the side of the pillars in a three-chamber device.
Tables S4. State transition function of FSA for the generation and degeneration of the DASH patterns at the static location.
Movie S1. Generation of the DASH patterns.
Movie S2. Generation of the DASH patterns (confocal laser scanning microscopy).
Movie S3. Overlay of time-lapse video and CFD simulation.
Movie S4. Sequential generation and degeneration behaviors by DASH.
Movie S5. Repeated generation and degeneration behaviors by DASH.
Movie S6. Locomotion behavior powered by DASH.
Movie S7. Racing behavior powered by DASH.
References (*55*–*57*)

REFERENCES AND NOTES

1. D. Elson, Metabolism of nucleic acids (macromolecular DNA and RNA). *Annu. Rev. Biochem.* **34**, 449–486 (1965).
2. I. Prigogine, G. Nicolis, Biological order, structure and instabilities. *Q. Rev. Biophys.* **4**, 107–148 (1971).
3. R. Lakes, Materials with structural hierarchy. *Nature* **361**, 511–515 (1993).
4. P. Fratzl, R. Weinkamer, Nature's hierarchical materials. *Prog. Mater. Sci.* **52**, 1263–1334 (2007).
5. A. Y. Chen, Z. Deng, A. N. Billings, U. O. S. Seker, M. Y. Lu, R. J. Citorik, B. Zakeri, T. K. Lu, Synthesis and patterning of tunable multiscale materials with engineered cells. *Nat. Mater.* **13**, 515–523 (2014).
6. P. Q. Nguyen, N.-M. D. Courchesne, A. Duraj-Thatte, P. Praveschotinunt, N. S. Joshi, Engineered living materials: Prospects and challenges for using biological systems to direct the assembly of smart materials. *Adv. Mater.* **30**, 1704847 (2018).
7. D. A. Fletcher, R. D. Mullins, Cell mechanics and the cytoskeleton. *Nature* **463**, 485–492 (2010).
8. T. Sanchez, D. T. N. Chen, S. J. DeCamp, M. Heymann, Z. Dogic, Spontaneous motion in hierarchically assembled active matter. *Nature* **491**, 431–434 (2012).
9. H. Hess, J. L. Ross, Non-equilibrium assembly of microtubules: From molecules to autonomous chemical robots. *Chem. Soc. Rev.* **46**, 5570–5587 (2017).
10. E. te Brinke, J. Groen, A. Herrmann, H. A. Heus, G. Rivas, E. Spruijt, W. T. S. Huck, Dissipative adaptation in driven self-assembly leading to self-dividing fibrils. *Nat. Nanotechnol.* **13**, 849–855 (2018).
11. G. M. Whitesides, B. Grzybowski, Self-assembly at all scales. *Science* **295**, 2418–2421 (2002).
12. R. Yoshida, T. Ueki, Evolution of self-oscillating polymer gels as autonomous polymer systems. *NPG Asia Mater.* **6**, e107 (2014).
13. R. M. Noyes, R. J. Field, Oscillatory chemical reactions. *Annu. Rev. Phys. Chem.* **25**, 95–119 (1974).
14. G. Loget, A. Kuhn, Propulsion of microobjects by dynamic bipolar self-regeneration. *J. Am. Chem. Soc.* **132**, 15918–15919 (2010).
15. B. Grzybowski, H. A. Stone, G. M. Whitesides, Dynamic self-assembly of magnetized, millimetre-sized objects rotating at a liquid-air interface. *Nature* **405**, 1033–1036 (2000).
16. M. Fialkowski, K. J. M. Bishop, R. Klajn, S. K. Smoukov, C. J. Campbell, B. A. Grzybowski, Principles and Implementations of Dissipative (Dynamic) Self-Assembly. *J. Phys. Chem. B* **110**, 2482–2496 (2006).
17. J. Palacci, S. Sacanna, A. P. Steinberg, D. J. Pine, P. M. Chaikin, Living crystals of light-activated colloidal surfers. *Science* **339**, 936–940 (2013).
18. S. Debnath, S. Roy, R. V. Ulijn, Peptide nanofibers with dynamic instability through nonequilibrium biocatalytic assembly. *J. Am. Chem. Soc.* **135**, 16789–16792 (2013).
19. J. Boekhoven, W. E. Hendriksen, G. J. M. Koper, R. Eelkema, J. H. van Esch, Transient assembly of active materials fueled by a chemical reaction. *Science* **349**, 1075–1079 (2015).
20. N. C. Seeman, DNA in a material world. *Nature* **421**, 427–431 (2003).
21. Y. H. Roh, R. C. H. Ruiz, S. Peng, J. B. Lee, D. Luo, Engineering DNA-based functional materials. *Chem. Soc. Rev.* **40**, 5730–5744 (2011).
22. D. Yang, M. R. Hartman, T. L. Derrien, S. Hamada, D. An, K. G. Yancey, R. Cheng, M. Ma, D. Luo, DNA materials: Bridging nanotechnology and biotechnology. *Acc. Chem. Res.* **47**, 1902–1911 (2014).
23. M. R. Jones, N. C. Seeman, C. A. Mirkin, Programmable materials and the nature of the DNA bond. *Science* **347**, 1260901 (2015).
24. E. Winfree, F. Liu, L. A. Wenzler, N. C. Seeman, Design and self-assembly of two-dimensional DNA crystals. *Nature* **394**, 539–544 (1998).
25. P. W. K. Rothemund, Folding DNA to create nanoscale shapes and patterns. *Nature* **440**, 297–302 (2006).
26. S. H. Um, J. B. Lee, N. Park, S. Y. Kwon, C. C. Umbach, D. Luo, Enzyme-catalysed assembly of DNA hydrogel. *Nat. Mater.* **5**, 797–801 (2006).
27. J. B. Lee, S. Peng, D. Yang, Y. H. Roh, H. Funabashi, N. Park, E. J. Rice, L. Chen, R. Long, M. Wu, D. Luo, A mechanical metamaterial made from a DNA hydrogel. *Nat. Nanotechnol.* **7**, 816–820 (2012).
28. N. Park, S. H. Um, H. Funabashi, J. Xu, D. Luo, A cell-free protein-producing gel. *Nat. Mater.* **8**, 432–437 (2009).
29. K. Lund, A. J. Manzo, N. Dabby, N. Michelotti, A. Johnson-Buck, J. Nangreave, S. Taylor, R. Pei, M. N. Stojanovic, N. G. Walter, E. Winfree, H. Yan, Molecular robots guided by prescriptive landscapes. *Nature* **465**, 206–210 (2010).
30. C. A. Mirkin, R. L. Letsinger, R. C. Mucic, J. J. Storhoff, A DNA-based method for rationally assembling nanoparticles into macroscopic materials. *Nature* **382**, 607–609 (1996).
31. A. P. Alivisatos, K. P. Johnsson, X. Peng, T. E. Wilson, C. J. Loweth, M. P. Bruchez, P. G. Schultz, Organization of "nanocrystal molecules" using DNA. *Nature* **382**, 609–611 (1996).

Downloaded from https://www.science.org at The Hong Kong University of Science and Technology (Guangzhou) on May 26, 2026

32. W. Cheng, M. J. Campolongo, J. J. Cha, S. J. Tan, C. C. Umbach, D. A. Muller, D. Luo, Free-standing nanoparticle superlattice sheets controlled by DNA. *Nat. Mater.* **8**, 519–525 (2009).
33. R. Murphy, *Introduction to AI Robotics* (MIT Press, 2000).
34. H. Y. Lee, H. Jeong, I. Y. Jung, B. Jang, Y. C. Seo, H. Lee, H. Lee, DhITACT: DNA hydrogel formation by isothermal amplification of complementary target in fluidic channels. *Adv. Mater.* **27**, 3513–3517 (2015).
35. Y. Huang, X. Duan, Q. Wei, C. M. Lieber, Directed assembly of one-dimensional nanostructures into functional networks. *Science* **291**, 630–633 (2001).
36. J. J. Benítez, J. Topolancik, H. C. Tian, C. B. Wallin, D. R. Latulippe, K. Szeto, P. J. Murphy, B. R. Cipriany, S. L. Levy, P. D. Soloway, H. G. Craighead, Microfluidic extraction, stretching and analysis of human chromosomal DNA from single cells. *Lab Chip* **12**, 4848–4854 (2012).
37. R. Rusconi, S. Lecuyer, N. Autrusson, L. Guglielmini, H. A. Stone, Secondary flow as a mechanism for the formation of biofilm streamers. *Biophys. J.* **100**, 1392–1399 (2011).
38. Y. Zheng, J. Chen, J. A. López, Flow-driven assembly of VWF fibres and webs in in vitro microvessels. *Nat Commun.* **6**, 7858 (2015).
39. J. T. Bonner, A descriptive study of the development of the slime mold dictyostelium discoideum. *Am. J. Bot.* **31**, 175–182 (1944).
40. Y.-C. Kwon, M. C. Jewett, High-throughput preparation methods of crude extract for robust cell-free protein synthesis. *Sci. Rep.* **5**, 8663 (2015).
41. S. M. Douglas, I. Bachelet, G. M. Church, A logic-gated nanorobot for targeted transport of molecular payloads. *Science* **335**, 831–834 (2012).
42. S. Murata, A. Konagaya, S. Kobayashi, H. Saito, M. Hagiya, Molecular robotics: A new paradigm for artifacts. *N. Gener. Comput.* **31**, 27–45 (2013).
43. M. Hagiya *et al.*, in *Unconventional Computation and Natural Computation* (Springer, 2014), vol. 8553 of *Lecture Notes in Computer Science*, pp. 177–189.
44. M. Hagiya, A. Konagaya, S. Kobayashi, H. Saito, S. Murata, Molecular robots with sensors and intelligence. *Acc. Chem. Res.* **47**, 1681–1690 (2014).
45. A. E. Marras, L. Zhou, H.-J. Su, C. E. Castro, Programmable motion of DNA origami mechanisms. *Proc. Natl. Acad. Sci. U.S.A.* **112**, 713–718 (2015).
46. A. Cangialosi, C. K. Yoon, J. Liu, Q. Huang, J. Guo, T. D. Nguyen, D. H. Gracias, R. Schulman, DNA sequence–directed shape change of photopatterned hydrogels via high-degree swelling. *Science* **357**, 1126–1130 (2017).
47. A. J. Thubagere, W. Li, R. F. Johnson, Z. Chen, S. Doroudi, Y. L. Lee, G. Izatt, S. Wittman, N. Srinivas, D. Woods, E. Winfree, L. Qian, A cargo-sorting DNA robot. *Science* **357**, eaan6558 (2017).
48. Y. Sato, Y. Hiratsuka, I. Kawamata, S. Murata, S.-i. M. Nomura, Micrometer-sized molecular robot changes its shape in response to signal molecules. *Sci. Robot.* **2**, eaal3735 (2017).
49. J. J. Keya, R. Suzuki, A. M. R. Kabir, D. Inoue, H. Asanuma, K. Sada, H. Hess, A. Kuzuya, A. Kakugo, DNA-assisted swarm control in a biomolecular motor system. *Nat Commun.* **9**, 453 (2018).
50. E. Kopperger, J. List, S. Madhira, F. Rothfischer, D. C. Lamb, F. C. Simmel, A self-assembled nanoscale robotic arm controlled by electric fields. *Science* **359**, 296–301 (2018).
51. S. Tibbits, K. Cheung, Programmable materials for architectural assembly and automation. *Assem. Autom.* **32**, 216–225 (2012).
52. P. H. Opgenorth, T. P. Korman, L. Iancu, J. U. Bowie, A molecular rheostat maintains ATP levels to drive a synthetic biochemistry system. *Nat. Chem. Biol.* **13**, 938–942 (2017).
53. L. S. Penrose, Self-reproducing machines. *Sci. Am.* **200**, 105–114 (1959).
54. Y. Sakatani, T. Yomo, N. Ichihashi, Self-replication of circular DNA by a self-encoded DNA polymerase through rolling-circle replication and recombination. *Sci. Rep.* **8**, 13089 (2018).
55. R. D. Blake, S. G. Delcourt, Thermodynamic effects of formamide on DNA stability. *Nucleic Acids Res.* **24**, 2095–2103 (1996).
56. T. T. Nguyen, K. L. Sly, J. C. Conboy, Comparison of the energetics of avidin, streptavidin, neutrAvidin, and anti-biotin antibody binding to biotinylated lipid bilayer examined by second-harmonic generation. *Anal. Chem.* **84**, 201–208 (2012).
57. M. Morpurgo, A. Radu, E. A. Bayer, M. Wilchek, DNA condensation by high-affinity interaction with avidin. *J. Mol. Recognit.* **17**, 558–566 (2004).

Acknowledgments: We thank M. P. DeLisa and M. C. Jewett for providing plasmids, J. Thompson and K. Lloyd Perry for providing CMV gene sequences, and J. Hunter for critical reading of the manuscript. S.H. thanks S. Tsai, F. Zhang, T. Chari, J. Li, R. Bollapragada, S. H. Chun, C. Min-Yi Costello, J. Popp, A. G. Samper, A. Stone, and R. Klein for assistance. **Funding:** M.G. and P.L. acknowledge support from the National Natural Science Foundation of China (21778071, 81472842, 81771968, and 31400087). M.G. acknowledges support from the Youth Innovation Promotion Association CAS (2015257) and the Suzhou Institute of Nano-Tech and Nano-Bionics (Y5AAS11001). We acknowledge financial support from the U.S. National Science Foundation (NSF) (EFRI-1331583 and SNM-1530522). S.H. and D.L. acknowledge support from the Kavli Institute at Cornell for Nanoscale Science. T.L.D. acknowledges support from the NSF IGERT (DGE-0903653). This work was performed, in part, at the Cornell NanoScale Science and Technology Facility, a member of the National Nanotechnology Coordinated Infrastructure, which is supported by the NSF (ECCS-1542081). This work made use of the Nanobiotechnology Center shared research facilities at Cornell, the Cornell Center for Materials Research shared facilities that are supported through the NSF MRSEC program (DMR-1120296), and facilities at Cornell College of Architecture, Art, and Planning. **Author contributions:** S.H. and D.L. created the concepts, designed the mechanism, performed the data analyses, and led the project. S.H., K.G.Y., Y.P., M.G., D.A., Y.H., T.L.D., and R.R. performed the experiments and data analyses. M.V. and J.S. performed the simulation. P.L., J.S., and D.L. supervised the authors. All authors contributed to the writing of the manuscript. **Competing interests:** S.H., K.G.Y., and D.L. declare competing interests (listed as inventors of a patent application filed by Cornell University). The remaining authors declare that they have no competing financial interests. **Data and materials availability:** All data needed to evaluate the conclusions in the paper are present in the paper or the Supplementary Materials. The source code for this study have been deposited on GitHub (https://github.com/nanobio/DASH-Analysis-MATLAB).

Submitted 11 December 2018
Accepted 20 February 2019
Published 10 April 2019
10.1126/scirobotics.aaw3512

Citation: S. Hamada, K. G. Yancey, Y. Pardo, M. Gan, M. Vanatta, D. An, Y. Hu, T. L. Derrien, R. Ruiz, P. Liu, J. Sabin, D. Luo, Dynamic DNA material with emergent locomotion behavior powered by artificial metabolism. *Sci. Robot.* **4**, eaaw3512 (2019).

Downloaded from https://www.science.org at The Hong Kong University of Science and Technology (Guangzhou) on May 26, 2026

Science Robotics

Dynamic DNA material with emergent locomotion behavior powered by artificial metabolism

Shogo Hamada, Kenneth Gene Yancey, Yehudah Pardo, Mingzhe Gan, Max Vanatta, Duo An, Yue Hu, Thomas L. Derrien, Roanna Ruiz, Peifeng Liu, Jenny Sabin, and Dan Luo

Sci. Robot. **4** (29), eaaw3512. DOI: 10.1126/scirobotics.aaw3512

View the article online
https://www.science.org/doi/10.1126/scirobotics.aaw3512
Permissions
https://www.science.org/help/reprints-and-permissions

Downloaded from https://www.science.org at The Hong Kong University of Science and Technology (Guangzhou) on May 26, 2026

Use of this article is subject to the Terms of service

Science Robotics (ISSN 2470-9476) is published by the American Association for the Advancement of Science. 1200 New York Avenue NW, Washington, DC 20005. The title *Science Robotics* is a registered trademark of AAAS.

Copyright © 2019 The Authors, some rights reserved; exclusive licensee American Association for the Advancement of Science. No claim to original U.S. Government Works